The Meteoritical Society

Meteoritics & Planetary Science 48, Nr 8, 1440–1458 (2013)
doi: 10.1111/maps.12158

Mg and Si isotopic fractionation patterns in types B1 and B2 CAIs: Implications for formation under different nebular conditions

Emma S. BULLOCK[1*], Kim B. KNIGHT[2], Frank M. RICHTER[3], Noriko T. KITA[4], Takayuki USHIKUBO[4], Glenn J. MACPHERSON[1], Andrew M. DAVIS[3,5], and Ruslan A. MENDYBAEV[3]

[1]US National Museum of Natural History, Smithsonian Institution, Washington, District of Columbia 20560, USA
[2]Lawrence Livermore National Laboratory, 7000 East Avenue, Livermore, California 94550–9234, USA
[3]Department of the Geophysical Sciences, University of Chicago, Chicago 60637, USA
[4]Department of Geosciences, University of Wisconsin-Madison, Madison, Wisconsin 53706, USA
[5]Enrico Fermi Institute, University of Chicago, Chicago 60637, USA
[*]Corresponding author. E-mail: bullockE@si.edu.

(Received 27 September 2012; revision accepted 10 June 2013)

Abstract–Magnesium and silicon isotopic profiles across melilite grains in two type B1 and two type B2 calcium-aluminum-rich inclusions (CAIs) reveal differing but constant enrichments in heavy isotopes everywhere except ≤1000 μm from the CAI margins. There is no close correlation in the B1s or the B2s between isotopic composition and åkermanite content of the melilite, a measure of progressive igneous crystallization, yet such a correlation might be expected in a type B2: without a melilite mantle (as in B1s) to seal the interior off and prevent further evaporation, the melt would have maintained communication with the external gas. These observations indicate a model in which B1s and B2s solidified under differing conditions. The B2s solidified under lower hydrogen pressures ($P_{H_2} \leq 10^{-4} - 10^{-5}$ bars) than did B1s ($P_{H_2} > 10^{-4}$ bars), so surface volatilization was slower in the B2s and internal chemical and isotopic equilibrium was maintained over the interval of melilite crystallization. The outermost zones of the CAIs (≤1000 μm from the edge) are not consistently enriched in heavy isotopes relative to the interiors, as might be expected from diffusion-limited surface evaporation of the melt. In all cases, the magnesium in the CAI margins is lighter than in the interiors. In one case, silicon in the margin also is lighter, but locally in some CAIs, it is isotopically heavier near the surface. If melt evaporation played a role in the formation of these outer zones, a later event in many cases caused isotopic re-equilibration with an external and isotopically near-normal reservoir.

INTRODUCTION

Many calcium-aluminum-rich inclusions (CAIs) solidified from melt droplets. Textures and high-precision measurement of ^{26}Al-^{26}Mg internal isochrons indicate that melting and remelting of CAIs was an ongoing process in the nebula that extended over at least 0.7 Ma prior to incorporation of the CAIs into their parent bodies (MacPherson et al. 2012). Experimental work and data from natural samples (e.g., Clayton et al. 1988; Davis et al. 1990; Grossman et al. 2000; Richter et al. 2002, 2007b) both show that such melting probably was accompanied by melt evaporation and loss of silicon and magnesium relative to more refractory aluminum and calcium. This process caused enrichment of the heavy isotopes of magnesium and silicon in the residual melt, according to the Rayleigh law (see Discussion for details):

$$R/R_0 = f^{(\alpha-1)} \quad (1)$$

The melt evaporative loss of magnesium and silicon is thought to be the cause of the deviation of CAI bulk compositions away from those predicted by equilibrium

condensation calculations (e.g., Grossman et al. 2000; Richter et al. 2002, 2007b). This idea has been especially invoked in the case of type B CAIs in CV3 chondrites (Clayton et al. 1985, 1988; Grossman et al. 2000, 2008; Richter et al. 2002, 2006, 2007b; Sugiura et al. 2004; Knight et al. 2009b), which are the most-studied of the "igneous" CAIs. Type B bulk compositions are depleted in magnesium and silicon with respect to equilibrium condensates (e.g., Grossman et al. 2000), and type Bs consistently show enrichment in the heavy isotopes of magnesium and silicon (Clayton et al. 1988). The degree of isotopic fractionation observed in type B CAIs, and the fact that it is not restricted to a near surface layer, requires evaporation from a melt, rather than from a solid (Davis et al. 1990).

Type B CAIs are divided into two main subtypes, known as type B1 and type B2 (Wark and Lovering 1977, 1982). A third variety, rarely called type B3 (Wark et al. 1987) but more generally known as forsterite-bearing inclusions (e.g., Clayton et al. 1985) or forsterite-bearing type Bs (e.g., Bullock et al. 2012), may or may not have any direct genetic relationship with the B1s/B2s and are not considered further herein. type B1 and type B2 CAIs are all coarse-grained and are or were (prior to any deformation) generally spheroidal in shape. type B1 inclusions are concentrically zoned, with thick, continuous melilite mantles surrounding cores of melilite + pyroxene + anorthite + spinel. The mantle may contain small grains of pyroxene and spinel. Type B2 inclusions lack a thick melilite mantle, and instead have a more or less uniform distribution of melilite + pyroxene + anorthite + spinel throughout.

The origin of the melilite mantle in type B1s, and conversely, the reason for its absence in type B2s, are debated. The B1 mantles originally were thought to be the simple consequences of melt bulk compositions that crystallized melilite early and singly over a prolonged temperature interval (MacPherson and Grossman 1981), in contrast to the B2s whose melts were nearly saturated with all phases at the onset of melt solidification. More recently, the B1–B2 differences have been ascribed to differing rates of melt evaporation of silicon and magnesium from the CAI surfaces (Mendybaev et al. 2006). Regardless, study of the melilite itself is key to resolving the problem. Melilite in CAIs is a simple binary solid solution between the endmembers gehlenite ($Ca_2Al_2SiO_7$) and åkermanite ($Ca_2MgSi_2O_7$), and the phase diagram has a thermal minimum at approximately $Åk_{72}$. In all melts more aluminous than this, the crystallizing melilite will start out aluminum-(gehlenite-) rich (typically approximately $Åk_{20}$ for type B-like compositions) and (neglecting minor complexities due to pyroxene preceding anorthite in the late crystallization sequence; MacPherson et al. 1984) become progressively more magnesium-rich until (if) reaching the minimum at approximately $Åk_{72}$. All type B1 and B2 melts fall into this category. Moreover, in both B1s and B2s melilite is a very early crystallizing phase (second only to spinel; Stolper 1982). Thus, melilite compositional zoning is a map to the early crystallizing history of the CAIs.

Richter et al. (2006) suggested that once a melilite mantle formed around a type B1 CAI droplet, evaporation of magnesium and silicon was suppressed and interior melilite grew in an effectively closed system. Thus, in a type B1, the melilite will would be zoned in åkermanite content, but the magnesium and silicon isotopic composition of the interior melilite would be approximately uniform (Mendybaev et al. 2006). Type B2 CAI melts, lacking an enclosing mantle, would have continued to evaporate during crystallization and melilite would have become increasingly isotopically heavy in magnesium and silicon as the åkermanite content increased during progressive crystallization. The aim of this work is to measure the magnesium and silicon isotopic fractionation of melilite as a function of melilite composition and location within type B1 and B2 CAIs, and thus to test the idea about what effect a mantle, or the lack thereof, had on the evolution of type B CAIs. A key idea is that in the type B1 CAIs, the isotopic fractionation should be approximately constant throughout the interiors of the inclusions (i.e., inside the mantles), whereas in the type B2s, one should expect a range of isotopic values and a more obvious and extended correlation between melilite åkermanite content and isotopic composition throughout the entire CAI.

Magnesium and silicon isotopes were measured in four different CAIs—two type B1 CAIs (Leoville USNM-*3535.1* and Allende *AL-4884*), and two type B2 CAIs—Allende *TS33-F1* and Vigarano *3138 F1*. Descriptions and high-precision ^{26}Al-^{26}Mg isotope analyses of Leoville USNM-*3535-1* and Vigarano *3138 F1* were reported by Kita et al. (2012) and MacPherson et al. (2012), respectively.

ANALYTICAL METHODS

Descriptions and Mineral Chemistry

Each thin section was studied petrographically using reflected and transmitted light optical microscopy, both to identify grain boundaries and to look for zoning within melilite crystals (in the simple binary melilite system, optical birefringence is a direct function of composition; see MacPherson 2007, for illustrations

of this). Quantitative major element chemical data were obtained using a JEOL JXA-8900R electron microprobe at the Smithsonian Institution, operating at 15 kV and 20 nA, and collected using proprietary ZAF/Phi-Rho-z programs for data reduction. Natural and synthetic minerals were used as both calibration and monitoring standards.

X-Ray Area Maps

Quantitative element maps of Mg, Al, Si, Ca, and Ti were made using the JEOL JSM-5800LV scanning electron microscope (SEM) at the University of Chicago, operated at 15 kV accelerating voltage. An Oxford ISIS energy dispersive analytical system was used both to collect the maps and then quantify each pixel using a proprietary standardless algorithm. The accuracy of quantification was checked against wavelength dispersive microprobe analyses of mapped melilite crystals. The element maps were then converted to maps of mole percent åkermanite in melilite, using the graphics program Igor (Wavemetrics, Inc.). These zoning maps were used to guide the choice of locations for isotopic analysis.

Isotopic Analyses

Isotopic data were collected using the Cameca IMS-1280 ion microprobe at the University of Wisconsin, Madison (WiscSIMS). Magnesium isotopic data were collected from melilite using a primary 5–8 nA O^- beam defocused to approximately 15 μm (Kohler illumination mode). Four Faraday cups (FC) enabled multicollection measurement of ^{24}Mg, ^{25}Mg, ^{26}Mg, and ^{27}Al. Detailed analytical conditions and SIMS instrument calibration methods are described in Kita et al. (2012). Silicon isotopes were measured with a Cs^+ primary beam focused to approximately 15 μm. Detailed analytical conditions are similar to those described in Knight et al. (2009a) and Heck et al. (2011). In earlier stages of the analysis, we measured three Si isotopes (^{28}Si, ^{29}Si, ^{30}Si) and ^{27}Al simultaneously using four multicollector FCs. Because no mass independent fractionation was observed, in the later part of the study we analyzed only ^{28}Si and ^{30}Si (plus ^{27}Al) under conditions similar to that reported by Heck et al. (2011) with lower primary intensities of 2–3 nA. Typical analytical precision for $\delta^{25}Mg$ and $\delta^{30}Si$ is 0.2–0.5‰, with relatively larger uncertainties for Al-rich and Mg- and Si-poor melilite. Instrumental mass fractionation of Mg and Si isotopes in melilite show well-defined linear correlations with $^{27}Al/^{24}Mg$ and $^{27}Al/^{28}Si$ ratios, respectively. The latter were calibrated using synthetic melilite glass standards with known Mg and Si isotope ratios. Similar calibration procedures were described in Knight et al. (2009a) and Kita et al. (2012).

After SIMS analysis, we obtained an SEM image of each ion probe pit to ensure that analyses were of a single phase, and to note locations where a beam overlap with cracks might have compromised the data. Such data were rejected.

Isotopic results are reported as deviations from a standard composition in parts per thousand (permil), using a conventional delta notation:

$$\delta^{25}Mg_{sample} = 1000\times\left[\left(^{25}Mg/^{24}Mg\right)_{sample}/\left(^{25}Mg/^{24}Mg\right)_{standard}-1\right] \quad (2)$$

$$\delta^{30}Si_{sample} = 1000\times\left[\left(^{30}Si/^{28}Si\right)_{sample}/\left(^{30}Si/^{28}Si\right)_{standard}-1\right] \quad (3)$$

RESULTS

General Descriptions

Leoville USNM-3535-1 (hereafter "*Leo 3535-1*") is an oval type B1 CAI, 0.6 × 0.8 cm, with distinctive fractures and terrestrial alteration veins cutting the CAI (Fig. 1). The melilite-dominated mantle is approximately 500 μm thick and contains dispersed spinel grains that in general are smaller than those in the CAI interior. The core is a well-mixed combination of melilite, fassaite, anorthite, and spinel. There is essentially no preterrestrial alteration (i.e., no nepheline, sodalite, grossular, etc.) present. The composition of melilite in *Leo 3535-1* is strongly dependent on the distance inward away from the surface of the CAI. The most aluminum-rich melilite ($Åk_{15–20}$) occurs within approximately 50 μm of the surface of the CAI (but note near the top of the image in Fig. 1 that microfaults locally have thrust aluminous melilite up to 100 μm underneath [interior to] more magnesium-rich melilite). Melilite becomes progressively more magnesium-rich inward, reaching a maximum of approximately $Åk_{83}$ (Mendybaev et al. 2007; Kita et al. 2012). Pyroxene in *Leo 3535-1* contains approximately 2–10% TiO_2 (calculated as Ti^{4+}; Kita et al. 2012).

Allende AL-4884 ("*AL-4884*"; Fig. 2) is an approximately 0.6 × 1.0 cm oval type B1 CAI with a heavily microfaulted surface. The core of *AL-4884* contains abundant coarse-grained melilite, fassaite,

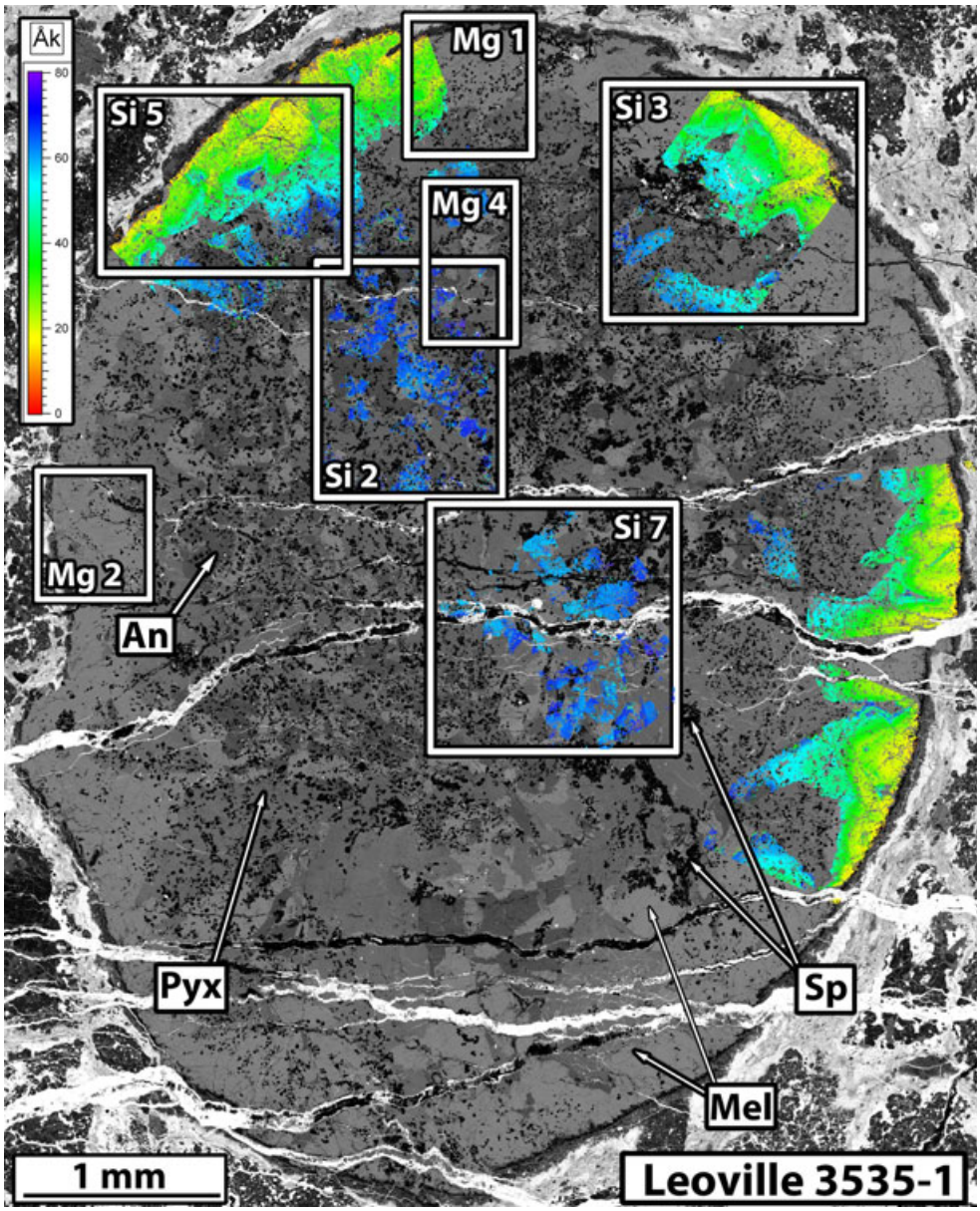

Fig. 1. Backscattered electron (BSE) image of *Leo 3535-1*, with colored quantitative maps of melilite åkermanite content (mole%) overlain on selected areas. The numbered rectangles correspond to the numbered areas designated on the isotopic profile diagrams in Figs. 5–8. For *Leo 3535-1* only, separate areas were analyzed for silicon and magnesium isotopes, and are so indicated. No such designation is required or give for the other three CAIs in Figs. 2–4. Early forming, gehlenitic melilite appears orange-yellow in this scale, and with progressive crystallization becomes more åkermanitic (green-dark blue). Thus, the melilite in this inclusion crystallized from the surface inward. The core of the inclusion contains the later-forming, åkermanitic melilite. Locations of individual analyses are given in the Supporting Information.

spinel, and minor anorthite. The melilite mantle (delineated by a dotted line on Fig. 2) is approximately 250–500 μm thick and, similar to *Leo 3535-1*, consists mainly of gehlenitic melilite + minor spinel. Melilite composition is a strong function of distance from the CAI outer surface, being approximately $Åk_{5–10}$ within approximately 50 μm of the surface but zoning inward to reach approximately $Åk_{71}$ in the CAI interior.

Typical of Allende CAIs, *AL-4884* contains abundant veins and patchy areas of secondary alteration. Pyroxene in *AL-4884* contains approximately 4.5–17.3% TiO_2 (calculated as Ti^{4+}) and 16.2–22.7% Al_2O_3.

Allende TS33 F1 ("*All TS33*") is an approximately 1.1 cm diameter round inclusion (Fig. 3) that was previously described by MacPherson and Grossman

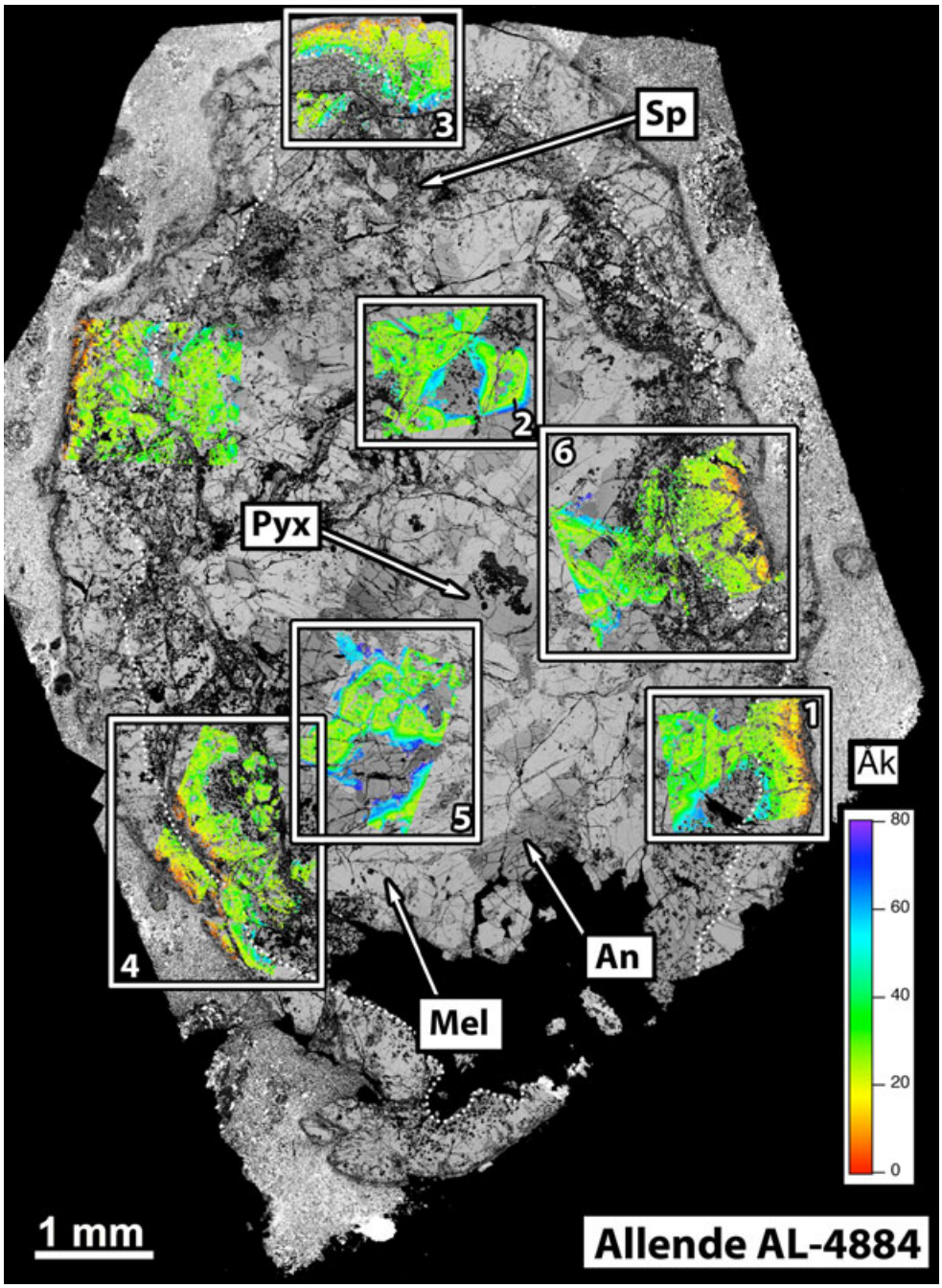

Fig. 2. Backscattered electron image of *AL-4884*, with colored maps of melilite åkermanite content for six analyzed areas overlain as in Fig. 1. This inclusion has a continuous melilite mantle of approximately $Åk_{10–30}$, indicated by a dotted line, suggesting it should be classified as a type B1 CAI. Locations of individual analyses are given in the Supporting Information.

(1981) and Simon et al. (1991). Only a portion (approximately 60%) of the CAI is present in the section studied—note in Fig. 3 that a Wark-Lovering rim surrounds the upper and left-hand portions of the CAI but is absent from the lower and right-hand regions, which form a broken surface. MacPherson and Grossman (1981) and Stolper (1982) considered *All TS33* to be a type B1 CAI, and its bulk composition led Beckett (1986) likewise to consider it as a type B1. Others, however, concluded that it is intermediate between a B1 and a B2 because although melilite is very enriched in the outer mantle, it does not form a continuous rind on the CAI (Simon et al. 1991). Probably, the latter classification is best but, for the

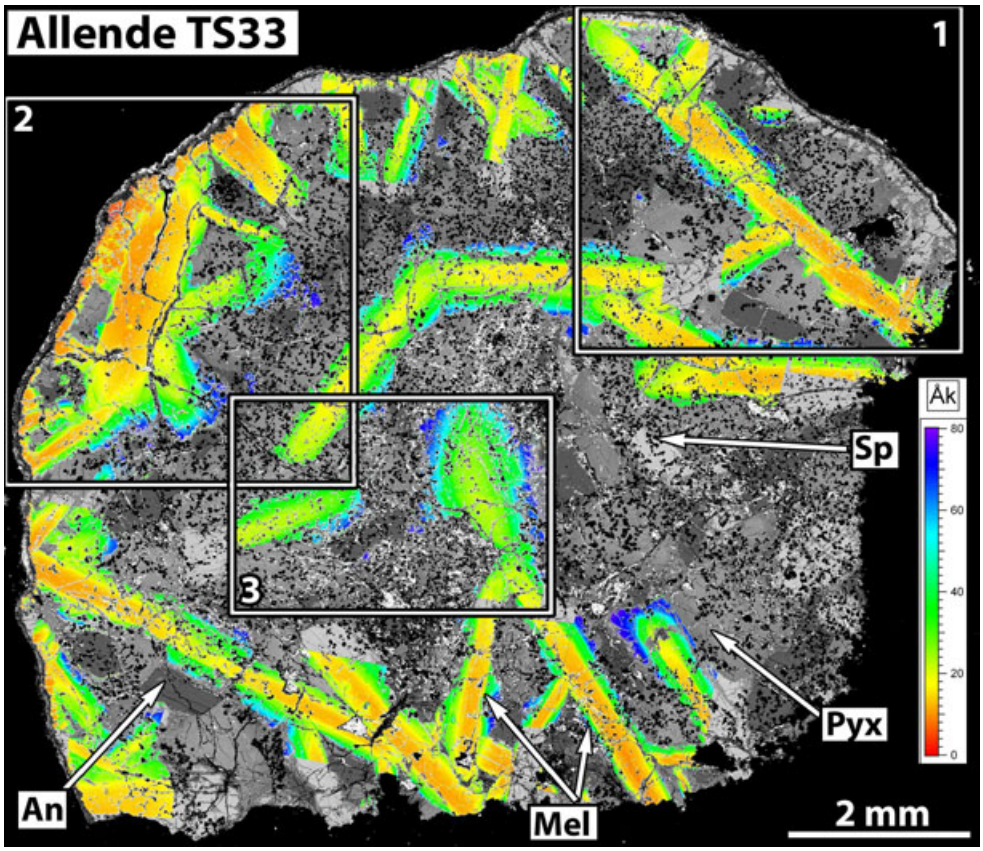

Fig. 3. Backscattered electron image of *All TS33* with colored maps of melilite åkermanite content for three analyzed areas overlain as in Fig. 1. Melilite crystallized simultaneously at the surface and in the core, as evidenced by grains in both locations having the same range of melilite compositions. Several grains crystallized inward from the edge. Locations of individual analyses are given in the Supporting Information.

primary purpose of this paper—testing whether a *continuous* melilite mantle shut off communication between the melt droplet and the surrounding gas—we can effectively treat *All TS33* as a type B2 CAI. *All TS33* consists of abundant euhedral laths of melilite and anhedral grains of fassaite that poikilitically enclose spinel grains. Anorthite is present but minor in abundance. The hallmark characteristic of *All TS33* is the radial orientation (axiolitic texture) of long melilite laths inward from the edge of the CAI. This, taken in combination with the fact that the laths become progressively more magnesium-rich along their lengths away from the CAI margin, demonstrates that melilite was an early crystallizing phase from a melt droplet that cooled from its outer surface (MacPherson and Grossman 1981). The compositions of melilite both within the core and toward the CAI margin are similar, with the lath centers typically being $Åk_{12–16}$ and the lath margins being $Åk_{60\text{-}70}$. However, within 100 μm of the outer surface of the CAI the melilite is very magnesium-poor, with $Åk < _{10}$. Pyroxene in *TS33* contains 5–11% TiO_2 (calculated as Ti^{4+}) and 19%–22% Al_2O_3 (MacPherson and Grossman 1981).

Vigarano 3138 F1 ("*Vig F1*") is an approximately 0.4 × 0.5 cm) oval inclusion. Two separate fragments of Vigarano *F1* were studied, designated *Vig F1a* and *Vig F1b*, and both are shown in Fig. 4. Melilite is abundant, and forms a nearly continuous, albeit very thin (<200 μm) outer mantle. Thus, classification of Vig-F1 is problematic in the same way as for *All-TS33*. However, because the "mantle" is so thin and not perfectly continuous, and also because melilite compositions are similar in the CAI core and outer regions, in the range $Åk_{15–73}$, we consider *Vig F1* to be a type B2. Unlike *All TS33*, the melilite in *Vig F1* is not monotonically zoned from aluminous cores to magnesian rims. Rather, the zoning is both somewhat oscillatory and patchy as can be seen in the melilite composition maps described below. Relatively aluminous zones toward the outer margins of some larger crystals are due to the onset of pyroxene crystallization prior to that of anorthite during melt

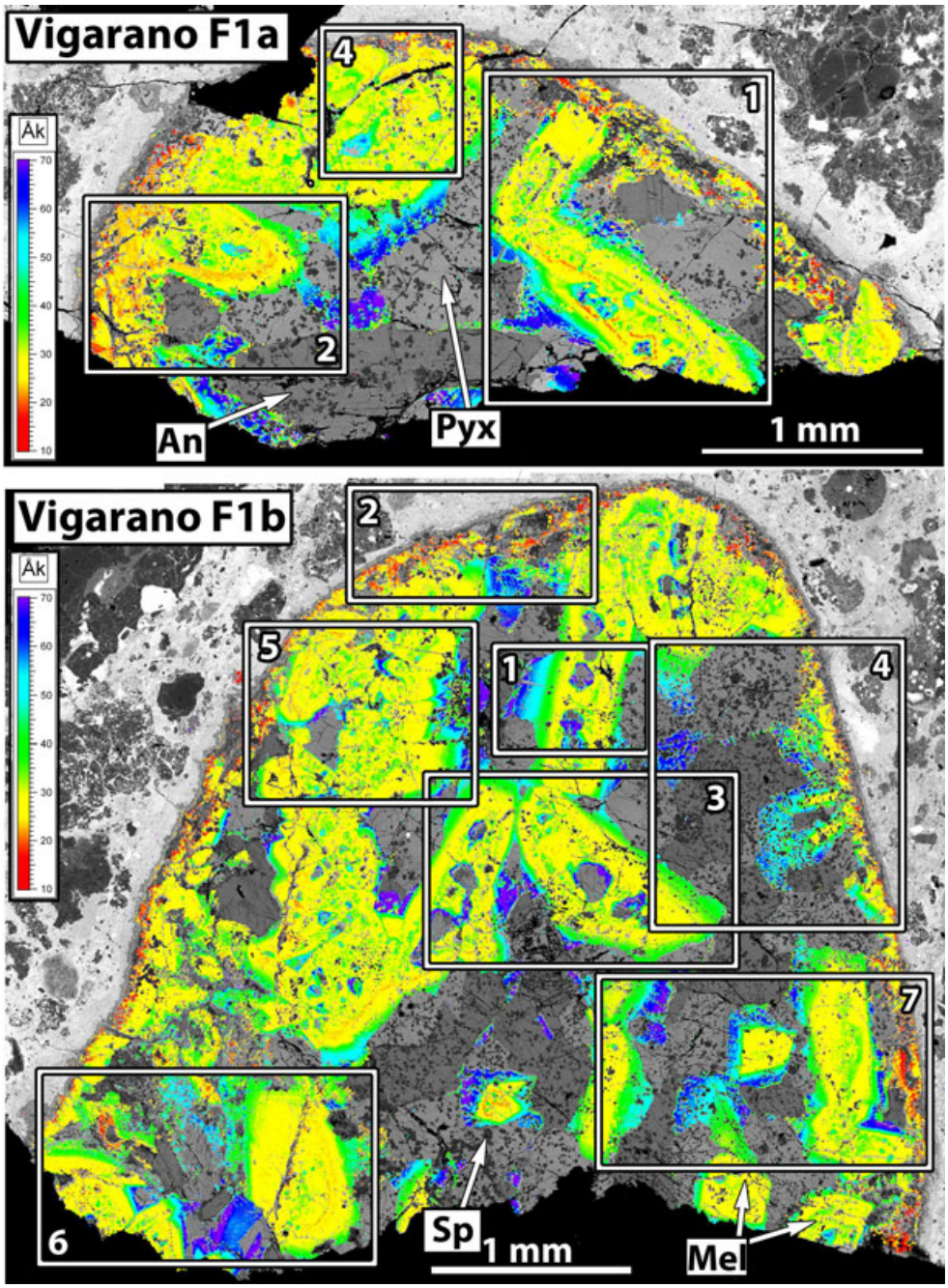

Fig. 4. Backscattered electron images of two sections of *Vig F1,* with colored maps of melilite åkermanite content for three (*Vig F1a*, top) and seven (*Vig F1b*, bottom) analyzed regions overlain as in Fig. 1. The scale in this image is expanded ($Åk_{10\text{-}70}$) to better illustrate the compositional zoning in the cores of melilite grains. There is a nearly continuous thin rind of gehlenitic melilite (red-orange) surrounding the inclusion, but the otherwise uniform distribution of melilite compositions elsewhere throughout the calcium-aluminum-rich inclusion indicates that *Vig F1* is best considered a type B2. Locations of individual analyses are given in the Supporting Information.

solidification, resulting in local reversed zoning (see MacPherson et al. 1984). Within 50–100 μm of the outer surface of the CAI the melilite is somewhat more aluminous, $Åk_{12\text{–}14}$. Course-grained pyroxene and anorthite are also present, and both phases (and melilite) enclose abundant spinel. Pyroxene in *Vig F1* contains 3.7–11.2% TiO_2 (calculated as Ti^{4+}) and 15.6–24.3% Al_2O_3. *Vig F1* is largely free of secondary alteration, but anorthite does contain fine lamellae of nepheline.

Melilite Composition Maps

To fully recognize the extent and nature of compositional zoning within melilite crystals prior to SIMS analysis, we made quantitative X-ray area maps of several representative regions within each CAI, in all cases including melilite crystals in the core, mantle, and outermost rim of each CAI. These in turn were converted to maps of mole% åkermanite, which served as the basis for deciding where to make isotopic profiles of Mg and Si isotopes. The colored maps, shown in Figs. 1–4, are each superimposed on a BSE image of the individual CAI. The numbered areas are identified by the red rectangles.

The melilite zoning map of *Leo 3535-1* is shown in Fig. 1, and demonstrates vividly the difference in composition between core and mantle melilite. Melilite ranges from $Åk_{16}$ at the outer edge to approximately $Åk_{55}$ at the mantle-core boundary. Melilite in the CAI core is uniformly more åkermanite-rich than that in the mantle, approximately $Åk_{55–76}$.

Melilite in *AL-4884* (Fig. 2) shows more complex zoning patterns than that in *Leo 3535-1* The melilite in the outermost approximately 100 μm of the mantle again is very aluminous ($Åk_{16–30}$) and becomes progressively more magnesium-rich inward toward the CAI core. The melilite in the core is consistently more magnesium-rich than that in the mantle approximately $Åk_{37}$–$Åk_{70}$, but many of these core crystals are more aluminous than their counterparts in *Leo 3535-1*. The zoning within each core crystal is not monotonic. Although in general the crystal centers are more aluminum-rich than the crystal rims (i.e., normally zoned, as expected from melt solidification), the zoning is very patchy and numerous magnesium-rich regions occur within the aluminum-rich cores.

The melilite zoning map (Fig. 3) for *All TS33* is striking. The long melilite laths dominate the texture, and each crystal is monotonically zoned from aluminum-rich cores to magnesium-rich rims. There is no patchy zoning like that seen in *AL-4884*. And, unlike the other inclusions in this study, aluminum-rich melilite is not confined to the mantle. However, it remains true here that the most aluminous melilite (approximately $Åk_8$) occurs within 100 μm of the mantle, and each lath that originates at the CAI surface becomes more magnesium-rich along its length and away from the CAI edge. Near the mantle-core interface, some of the long laths terminate at a composition of approximately $Åk_{70}$, near that of the melilite binary minimum. The range of åkermanite zoning in melilite grains in the interior of *All TS33* is similar to that of grains nearer the surface, $Åk_{15–70}$, indicating that some early melilite nucleation occurred in the interior of the CAI. Nonetheless, the overall melilite textures and zoning patterns in this CAI are suggestive that most melilite nucleation began on the outer surface of the CAI and progressed inward (MacPherson and Grossman 1981).

Melilite in *Vig F1* (Fig. 4) is similar in its zoning patterns to that in *AL-4884*. The very thin, nearly continuous melilite mantle contains the most aluminous melilite (approximately $Åk_{8–10}$), whereas the melilite elsewhere in the inclusion is more magnesium-rich, approximately $Åk_{25–73}$. The interior melilite maps shows "patchy" zoning like that in *AL-4884* (note that the mole% Åk scale in Fig. 4 has been stretched more than in Fig. 2 to better show the zoning from $Åk_{20–40}$ in the centers of the grains). Melilite in *Vig F1* encloses grains of pyroxene. Because the bulk composition of *Vig F1* is such that melilite should begin crystallizing prior to pyroxene, the enclosed pyroxenes suggest either melt entrapment during melilite growth or else trapping of relict pyroxene grains from a previous episode of melting and solidification.

Magnesium and Silicon Isotopes

Magnesium and silicon isotope data are shown graphically in Figs. 5–8, and tabulated in the Supporting Information. For each CAI, five graphs are shown: δ^{25}Mg plotted versus radial distance of the analysis spot from the CAI edge (top left), δ^{25}Mg plotted versus melilite åkermanite content of the analyzed spot (middle left), the same two graphs for δ^{30}Si (top right and middle right), and a plot of åkermanite content versus radial distance from the CAI edge for all spots (bottom left). See the Supporting Information for the locations of all analysis spots.

Leo 3535-1

Because the åkermanite content of melilite in Leo *3535-1* varies approximately linearly with distance from the CAI margin, there is a close correspondence between those isotope graphs plotted versus distance and those plotted versus åkermanite content (Fig. 5). Magnesium and silicon isotopes behave differently from one another in this CAI. Inward of about 500 μm from the CAI surface, both isotopes are approximately constant in abundance toward the inclusion core. δ^{25}Mg is enriched (relative to normal) by up to approximately 5‰ in the interior of the CAI where the melilite is magnesium-rich, but decreases progressively beginning about 500 μm from the CAI surface toward the actual surface, where δ^{25}Mg is only approximately 2–3‰ in the most aluminous melilite within approximately 100 μm of the CAI edge. Silicon isotopes are inconsistent. δ^{30}Si is strongly enriched by up to approximately 4.5‰ in some melilite grains within

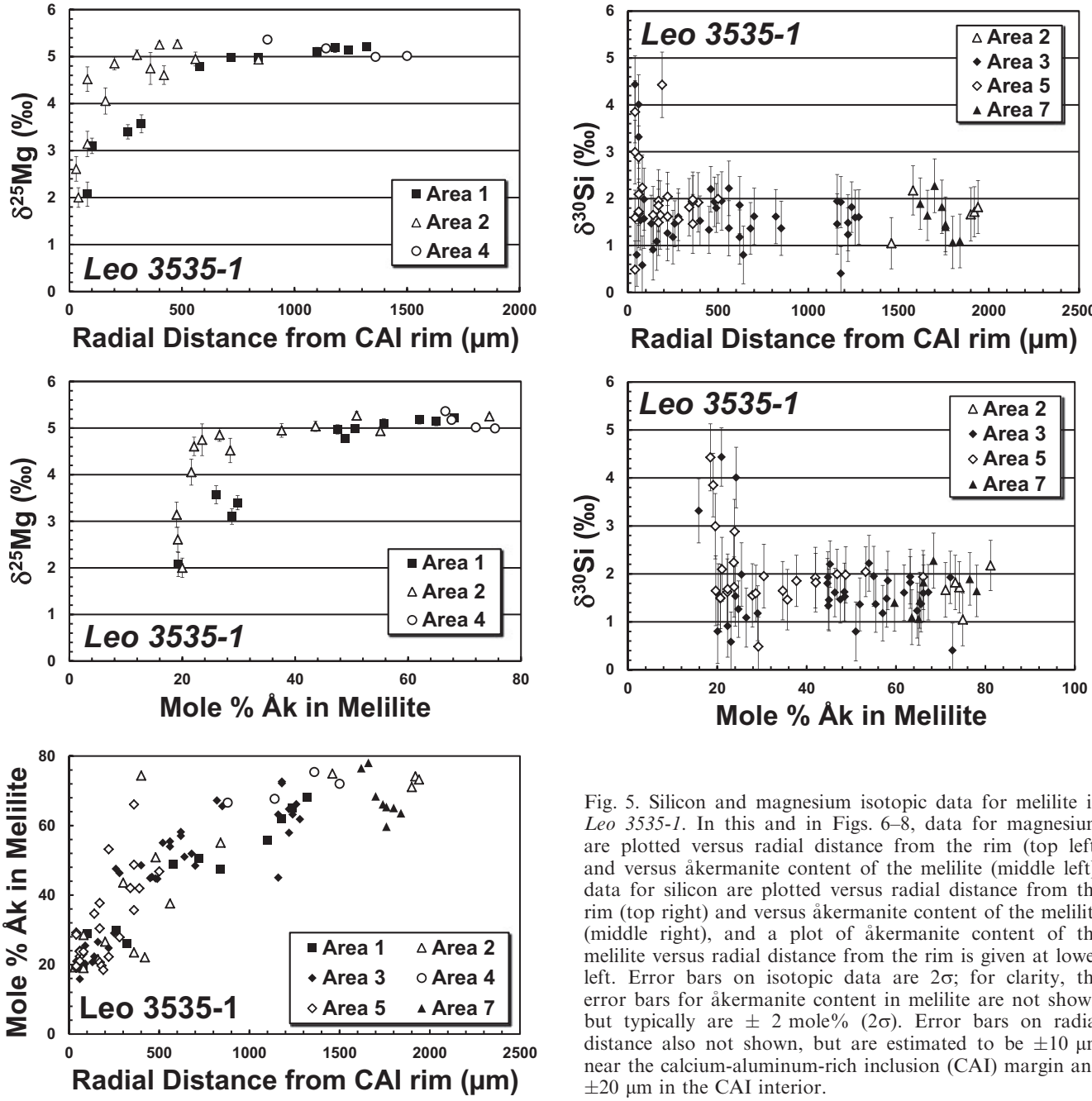

Fig. 5. Silicon and magnesium isotopic data for melilite in *Leo 3535-1*. In this and in Figs. 6–8, data for magnesium are plotted versus radial distance from the rim (top left) and versus åkermanite content of the melilite (middle left), data for silicon are plotted versus radial distance from the rim (top right) and versus åkermanite content of the melilite (middle right), and a plot of åkermanite content of the melilite versus radial distance from the rim is given at lower left. Error bars on isotopic data are 2σ; for clarity, the error bars for åkermanite content in melilite are not shown but typically are ± 2 mole% (2σ). Error bars on radial distance also not shown, but are estimated to be ±10 μm near the calcium-aluminum-rich inclusion (CAI) margin and ±20 μm in the CAI interior.

approximately 200 μm of the CAI margin, but inward of that distance, it remains about constant at approximately 1–2‰ into the CAI center. Note, however, that other melilite analysis spots very close to the CAI margin show no enrichment in δ^{30}Si relative to the CAI center. There is no correlation between isotopic enrichment and åkermanite content of the melilite anywhere except within several hundred μm of the outermost CAI surface. Our data for δ^{30}Si are similar to the results obtained by Shahar and Young (2007) on a compact type A CAI, although our data show a somewhat larger isotopic range. However, in the CAI analyzed by Shahar and Young (2007) the δ^{25}Mg directly mimics the δ^{30}Si and is enriched within 200 μm of the CAI margin relative to the interior, whereas in *Leo 3535-1,* the δ^{30}Si and δ^{25}Mg behave oppositely. Kita et al. (2012) showed that *Leo 3535-1* preserves a very well-defined Al-Mg isochron, implying that the magnesium isotopic systematics have not been disturbed by postcrystallization redistribution.

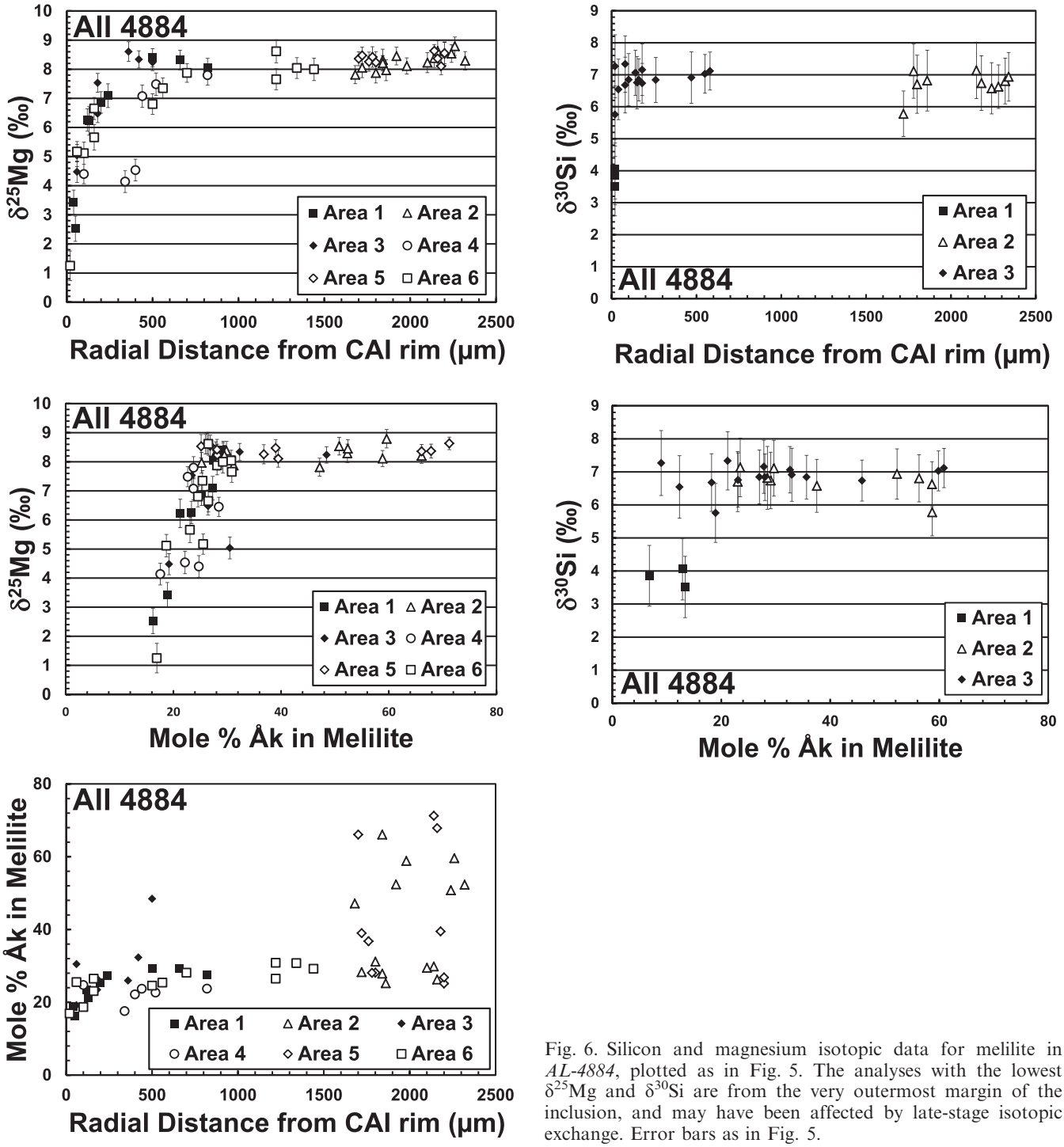

Fig. 6. Silicon and magnesium isotopic data for melilite in *AL-4884*, plotted as in Fig. 5. The analyses with the lowest δ^{25}Mg and δ^{30}Si are from the very outermost margin of the inclusion, and may have been affected by late-stage isotopic exchange. Error bars as in Fig. 5.

AL-4884

Unlike *Leo 3535-1*, the åkermanite content of melilite in *AL-4884* is not a simple linear function of distance from the CAI margin, which is why there is not such a close correspondence between those isotope graphs plotted versus distance and those plotted versus åkermanite content (Fig. 6). Especially this is true for δ^{30}Si. δ^{25}Mg is enriched at approximately constant levels (approximately 7.5–8.5‰) throughout the CAIs except within approximately 500 μm of the CAI margin, at which distance it decreases out to the CAI edge where it is as low as 1.2‰. However, as in the case of *Leo 3535-1*, δ^{30}Si does not show such a clear pattern. It is enriched at approximately constant

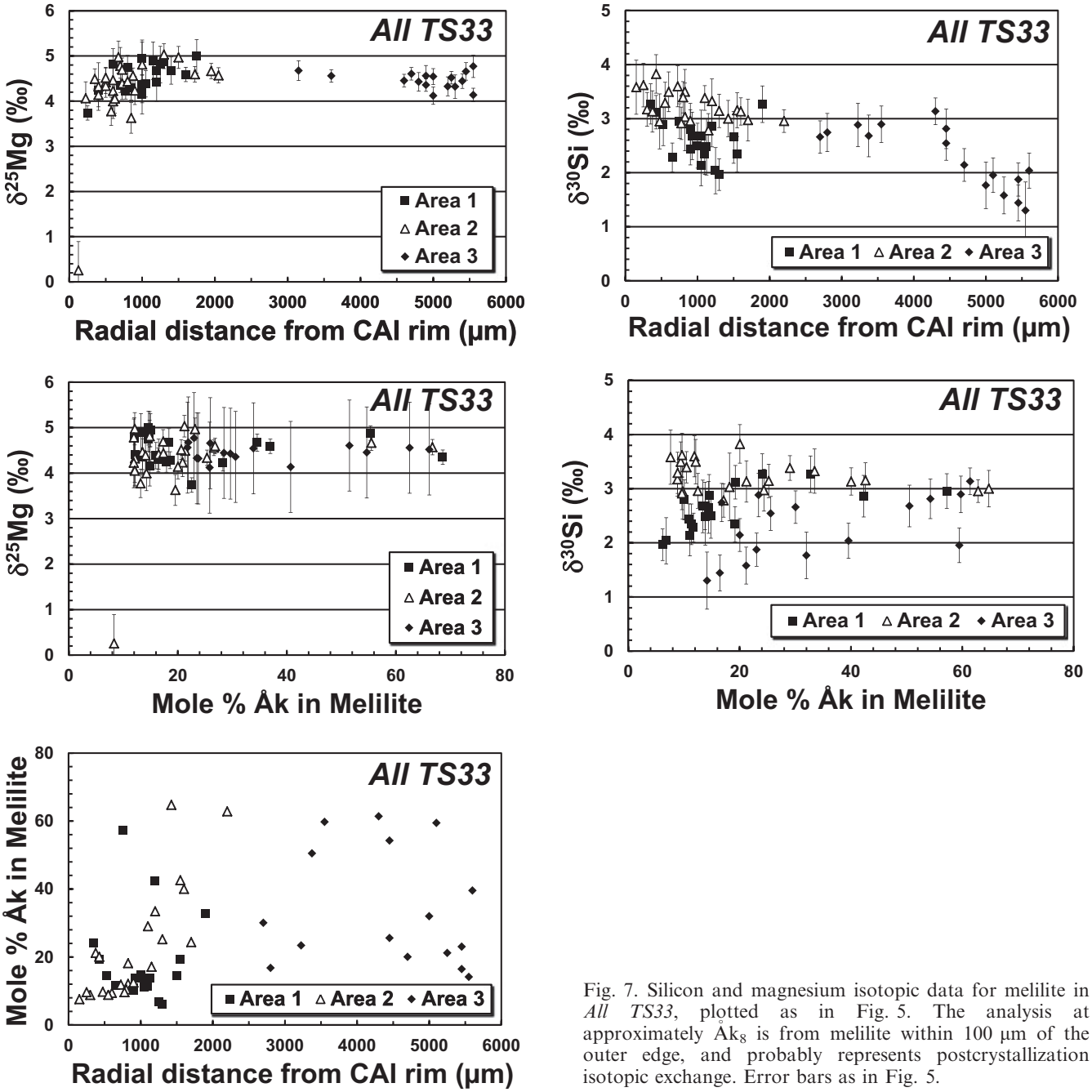

Fig. 7. Silicon and magnesium isotopic data for melilite in *All TS33*, plotted as in Fig. 5. The analysis at approximately $Åk_8$ is from melilite within 100 μm of the outer edge, and probably represents postcrystallization isotopic exchange. Error bars as in Fig. 5.

levels (approximately 6–7‰) throughout the CAIs except within approximately 100 μm of the CAI margin, where in some cases, it is depleted (approximately 3.5–4‰) relative to the CAI interior and in other places it is at the same level as in the CAI interior. The interior enrichment levels of both isotopes are significantly higher than those in *Leo 3535-1*. As in *Leo 3535-1*, there is no correlation between isotopic enrichment and åkermanite content of the melilite anywhere except within 200–500 μm of the CAI outer edge.

All TS33

The plot of radial distance versus the åkermanite content of melilite in *All TS33* (Fig. 7, lower left) shows that there is no correlation between the two parameters. This lack of correlation was also observed in another type B inclusion, "SH-1," by Sugiura et al. (2004; see also Mendybaev et al. 2007). Accordingly, the graphs showing isotopic enrichment plotted versus distance are different from those plotted versus åkermanite content, especially for $\delta^{30}Si$. As is true for all of the CAIs we analyzed, both $\delta^{25}Mg$ and $\delta^{30}Si$ are consistently heavy

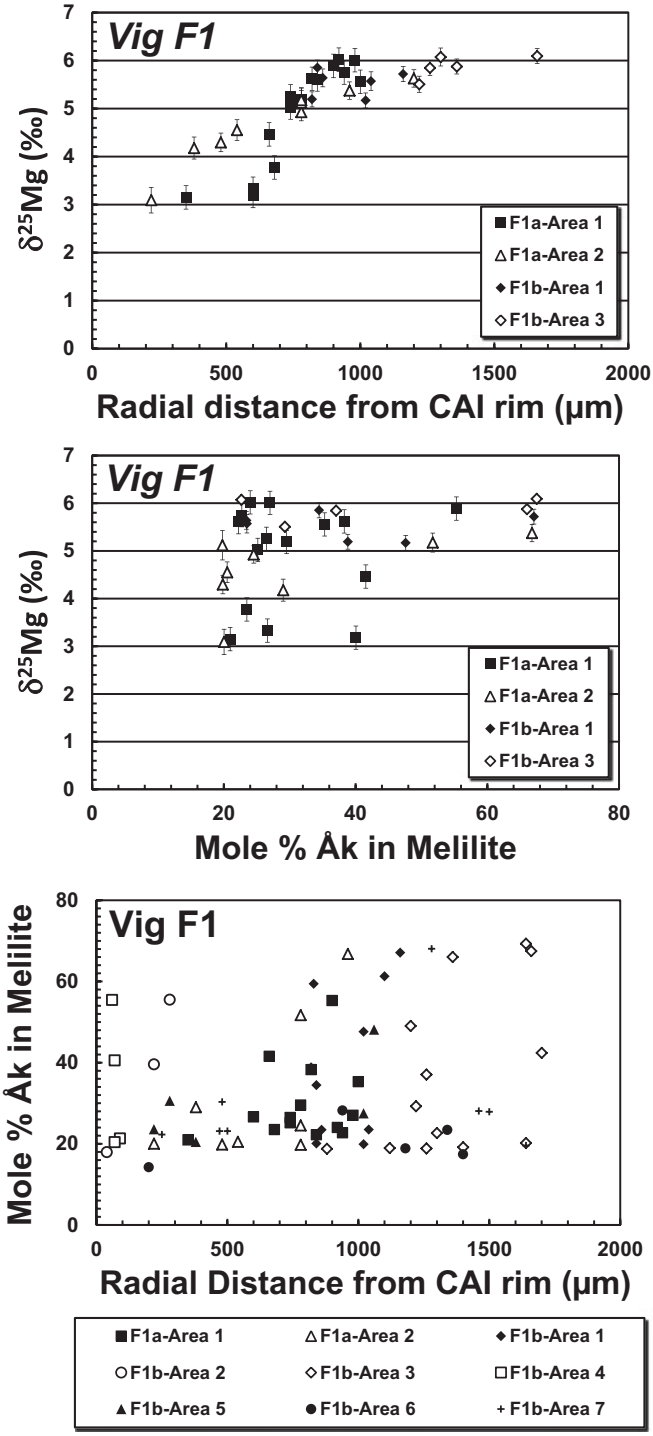

Fig. 8. Silicon and magnesium isotopic data for melilite in *Vig F1*, plotted as in Fig. 5. The two analyses within 200 μm of the outer edge are from the gehlenitic rind around the inclusion. Error bars as in Fig. 5.

at near-constant levels throughout the interior of this inclusion, but vary systematically between the outermost CAI surface and about 1 mm inward from the edge. Similar to *Leo 3535-1*, δ^{25}Mg and δ^{30}Si behave differently from one another. As a function of radial distance, δ^{25}Mg is mostly flat (4–5‰) throughout the inclusion except for a few locations within about 1 mm of the CAI margin that are slightly depleted (3.5–4‰) relative to the CAI interior. One analysis from <100 μm away from the rim of the inclusion has no detectable enrichment of δ^{25}Mg (0.3 ± 0.6‰); this is from the most aluminous melilite (Åk $\sim$ 8) in the CAI, but other than this one point, there is virtually no relationship between δ^{25}Mg and the åkermanite content in the melilite. The behavior of δ^{30}Si in *All TS33* is unusual relative to the other three CAIs. Overall, there

is a trend from being enriched (3–4‰) within about 1000 μm of the inclusion margin and less enriched (approximately 1.2‰) in the inclusion core, but in detail, the situation is somewhat more complicated. Only the melilite in Area 2 shows an enrichment pattern approaching the inclusion margin, whereas Area 1 shows only scatter. Area 3 is approximately constant at approximately 2.5–3.2‰ between 3000 and 4500 μm away from the CAI edge, then shows a progressive depletion down to approximately 1.4‰ between 4500 μm and 5500 μm (the CAI core). Note (Fig. 3) that Area 1 and Area 2 are both located about the same distance away from the CAI margin, yet their overall enrichments differ by about 1‰. Plotted as a function of åkermanite content of melilite, there is no consistent pattern for δ^{30}Si enrichment. Area 3 consists of two crystals that overlap those in Areas 1 and 2 in åkermanite content except at the most aluminum-rich extreme, yet the overall isotopic enrichment in Area 3 is consistently lower than in the other two areas. Area 1 shows a slight enrichment in δ^{30}Si at $Åk_{5–20}$ relative to the more magnesium-rich (>$Åk_{20}$) compositions, yet Area 2 shows the opposite effect.

F1

As in *All TS33*, a plot (Fig. 8, lower left) of radial distance versus the åkermanite content of melilite in *Vig F1* shows no correlation between the two parameters. Once again, therefore, the graphs (Fig. 8) showing isotopic enrichment plotted versus distance are different from those plotted versus åkermanite content. In *Vig F1* as in *All TS33* and *Leo 3535-1*, δ^{25}Mg and δ^{30}Si behave differently near the CAI margin, the former being depleted and the latter being enriched relative to the CAI interior. Plotted as a function of distance, δ^{25}Mg enrichment increases from approximately 3‰ at approximately 200 μm from the CAI edge to approximately 6‰ at 1000 μm away from the CAI edge, then remains constant into the CAI core. We were not able to get any clean analyses of δ^{25}Mg from within 200 μm of the CAI margin where the most aluminous melilite is located. For the data set we did get, there is no correlation at all between δ^{25}Mg and åkermanite content in the melilite. As in the other three CAIs, δ^{30}Si is not consistent. Two spots within approximately 200 μm of the CAI margin are enriched to 8–8.7‰, but otherwise δ^{30}Si is approximately constant at 4–7‰ throughout the CAI. There is little correlation between δ^{30}Si and åkermanite content in the melilite except that the most enriched spots also happen to be from aluminous melilite (and both within 100 μm of the CAI edge).

High-precision ^{26}Al-^{26}Mg isotope analyses of *Vig F1* were reported by MacPherson et al. (2012), and the melilite together with the pyroxene define a coherent isochron corresponding to initial $^{26}Al/^{27}Al = (4.66 \pm 0.17) \times 10^{-5}$; anorthite and some spinel are reset. Thus, the melilite isotopic properties in this CAI have not been disturbed by later reheating.

Pyroxene Analyses

Magnesium isotopic data were collected from pyroxene grains in the type B2 inclusions *Vig F1* and *All TS33*. In both inclusions, the values for δ^{25}Mg in pyroxene are very similar to the range seen within melilite grains in the interiors of the CAIs: δ^{25}Mg 4.3–5.0‰ in *All TS33* and 5.3–6.1‰ in *Vig F1*. Data are given in the Supporting Information.

DISCUSSION

The Effect of B1 Melilite Mantles on Isotopic Fractionation During Crystallization

The conventional interpretation of the mantles on type B1 CAIs is that, because B1s are more melilite-rich than are B2s (Beckett 1986), there is a greater temperature interval over which only melilite and spinel crystallized from the cooling melt droplet and this led to the formation of the melilite mantle. However, this idea does not take into account the fact that thermal equilibration in a molten 1-cm droplet would be so rapid that temperature gradients would not persist. More recently, Mendybaev et al. (2006) showed experimentally that differing rates of surface volatilization of magnesium and silicon from the molten droplets, under reducing conditions, could have caused the difference between B1s and B2s. Synthetic CAI melts maintained under reducing conditions (log fO_2 < IW-5) in a 1-atmosphere furnace experienced fast surface volatilization that exceeded the rate of internal liquid diffusion, leading to local depletion in silicon and magnesium at the surface, which raises the crystallization temperature of melilite and thus melilite crystallization would start at the surface to form the B1 mantle. The experiments also showed that under more oxidizing conditions, melilite does not form a mantle, but instead it crystallizes uniformly within the sample. This work was the basis for the prediction by Richter et al. (2006), and tested in the present paper, that the B1 mantles would serve to effectively shut off surface volatilization once the interior melt was sealed off from contact with the gas. Thus, the interiors of B1s effectively would have been closed systems in which the individual crystallizing melilite grains became zoned in åkermanite content but were uniform in their degree of isotopic fractionation. In the case of B2 inclusions, with

no sealing by melilite mantles, the melt continued to evaporate as the droplet cooled and crystallized melilite. In this case, the melilite crystals could have become increasingly isotopically heavy with progressive crystallization, and thus one would expect a correlation between increasing åkermanite content of the melilite crystals and increasingly heavy silicon and magnesium isotopic composition.

In light of the above, the most important result of our work is that in most of the CAIs, we analyzed (B2 as well as B1), the interiors (more than 0.2–1 mm away from the edge) of the inclusions are essentially constant in isotopic composition when plotted versus distance from the CAI margins. One B2 CAI, *All TS33*, actually shows a slight decrease in δ^{30}Si in the innermost portion of the CAI. Also, in general the degree of isotopic fractionation does not track the åkermanite content of melilite except to the extent that the åkermanite content is a direct function of distance from the CAI margin. Surprisingly, the isotopic gradients in the outer zones of the CAIs are not always in the direction of being heaviest at the margin. In three of the CAIs, magnesium and silicon do not even behave in the same sense, with silicon being more enriched near the margins and magnesium being less enriched relative to the CAI interiors.

In the interiors of all of the CAIs we analyzed, the melilite is isotopically heavy with respect to both silicon and magnesium, although to differing extents among the CAIs (and notably the inner core of *All TS33*). The B1 inclusion *AL-4884* shows the greatest degrees of enrichment in the heavy isotopes, with δ^{25}Mg approximately 8‰ and δ^{30}Si approximately 7‰ in the CAI interior (Fig. 7) and decreasing in the outer margin of the CAI. The other B1 inclusion, *Leo 3535-1,* shows smaller isotope fractionations; δ^{25}Mg approximately 5‰ and δ^{30}Si approximately 2‰ in the CAI interior (Fig. 5) and again decreasing outward. The interiors of the B2 inclusions *All TS33* and *Vig F1* show similar levels of enrichment to *Leo 3535-1* (Figs. 7 and 8), but in both CAIs the δ^{25}Mg enrichment decreases outward to the CAI edge, whereas the δ^{30}Si enrichment in *All TS33* seems to increase outward. The consistent enrichments of δ^{25}Mg and δ^{30}Si in the CAI interiors are evidence that significant amounts of magnesium and silicon were evaporated during one or more melting events. We use the kinetic fractionation factor $\alpha = 0.991$ for ^{25}Mg/^{24}Mg evaporated at 1400 °C (Richter et al. 2007) to estimate the amount of magnesium lost as 1-f with $f = (R/R_o)^{(\alpha-1)}$, where f is the fraction of magnesium remaining in a sample $R = {}^{25}\text{Mg}/{}^{24}\text{Mg}$, and R_o is the unfractionated isotope ratio (see Equation 7 below). This results in the estimates that *All TS33* lost approximately 39% of its magnesium, *Leo 3535-1* lost approximately 42%, *AL-4884* lost approximately 64%, and *Vig F1* lost approximately 46%. We use the kinetic isotopic fractionation factor $\alpha = 0.9804$ given by Knight et al. (2009a) in the same way to estimate the loss of silicon from the degree of ^{28}Si/^{30}Si fractionation of each CAI. This results in estimated losses of silicon of approximately 14% from *All TS33,* of approximately 8% from *Leo 3535-1,* of approximately 29% from *AL-4884*, and approximately 22% from *Vig F1*.

An inescapable conclusion from the results summarized above is that our data do not support the prediction of Richter et al. (2006) that types B1 and B2 CAIs should contain different internal isotopic fractionation patterns owing to the formation of melilite mantles in B1s and the absence of such a mantle in B2s. Specifically, the prediction is that the melilite crystals in type B2s, but not in type B1s, should show increasingly heavy isotope fractionation as a function of increasing åkermanite content (i.e., progressive crystallization) and this is not observed. Therefore, although the Richter et al. (2006) model may hold for the type B1s, something else needs to be taken into account to explain the B2s. We explore the latter problem below.

Implications for the Different Thermal Histories of type B2 versus type B1 CAIs

The flat profiles in the interiors of our CAIs require that isotopic diffusion in the melt outpaced the rate of surface evaporation, such that no internal isotopic gradients were preserved (neglecting the outermost margins, which is discussed separately below).

Shahar and Young (2007) made isotopic measurements similar to ours on a compact type A CAI. Like us, they found that the isotopic profiles for δ^{25}Mg and (in their case) δ^{29}Si are flat in the CAI interior, with a gradient present only in the outer 200 μm of the inclusion. Unlike the CAIs we analyzed, theirs showed elevated isotopic fractionation for both δ^{25}Mg and δ^{29}Si in the outermost margin relative to CAI interior (i.e., positive gradients outward). Their theoretical modeling successfully reproduced the flat profiles of the interior under melt evaporation conditions of $P_{H_2} < 10^{-6}$ bar. At higher pressures (e.g., 10^{-4} bar), they could not reproduce the overall level of isotopic enrichment. Although their models also showed that mild gradients could be preserved in the outer parts of the CAI, they could not reproduce the sharp gradients such as observed in their CAI or in ours. Their model is consistent with our observation that the isotopic fractionation in the interiors of all four CAIs is independent of a wide range of melilite composition, from Åk_{20} to Åk_{75}. This implies that evaporation and associated isotopic fractionation must have taken place before the crystallization of the melilite now in the

inclusion. This could have happened in one melting episode, in which case the evaporation must have occurred before melilite began to crystallize, or there were multiple evaporation events and that the final melting event completely dissolved all previous melilite and then cooled in such a way that there was very little further evaporation while the melilite now in the CAI crystallized.

We approach the problem from a different perspective than Shahar and Young (2007), by considering the conditions that might result in fractionated but more or less uniform silicon and magnesium isotopic composition of melilite in the interiors of both type B1 and type B2 CAIs. Also, our modeling is guided by the experimental petrology results of Mendybaev et al. (2006) that were specifically aimed at understanding the differences between types B1 and B2 CAIs.

Laboratory experiments suggest that type B1 and type B2 solidified under rather different conditions. Most experiments where melilite is crystallized from a CAI-like melt are performed at cooling rates of 50 °C h^{-1} or less. They generally produce type B2-like textures with euhedral to subhedral melilite crystals and no melilite mantle (e.g., Stolper and Paque 1986). The laboratory experiments of Mendybaev et al. (2006) showed that the type B2-like textures are produced when the silicon and magnesium evaporation from the surface of the molten droplet is negligible (as in the experiments by Stolper and Paque 1986) or when the evaporation rate is sufficiently slow compared with magnesium and silicon diffusion rates in the melt that the melt remains chemically homogeneous. Crystallization of such a melt would result in formation of melilite crystals more or less uniformly distributed within the sample. In contrast, Mendybaev et al. (2006) also showed that type B1-like textures result when the evaporation rate of silicon and magnesium is sufficiently fast compared with their diffusion in the melt that the surfaces of the samples become depleted in silicon and magnesium compared to the interior. Under these conditions, more gehlenitic melilite mantle starts first to crystallize in the outer portions of the samples followed by crystallization of more åkermanitic melilite in the central magnesium- and silicon-richer parts at lower temperatures. Thus, even though the melt droplet remains isothermal everywhere, the outer margin is effectively undercooled relative to the melilite crystallization temperature whereas that in the interior is not. The chief difference between the two sets of experiments is the rate of evaporation relative to that of diffusion. Increasing the hydrogen pressure increases the evaporation rate, but not the rate of diffusion, so, the type B1 texture will arise when the hydrogen pressure is relatively high, whereas the B2 texture will occur at lower hydrogen pressures.

Mendybaev et al. (2006) used the dependence of the evaporation rate of silicon and magnesium as a function of hydrogen pressure (e.g., fig. 12 in Richter et al. 2002) to argue that hydrogen pressures (P_{H_2}) greater than approximately 10^{-4} bars would be required for evaporation to be sufficiently fast that diffusion could not maintain homogeneity and thus a type B1-like mantle would be produced as the inclusion cooled. At lower hydrogen pressures ($P_{H_2} \leq 10^{-5}$ bars), the evaporation rate would be sufficiently slow that chemical diffusion would be able to maintain a uniform composition throughout the melt and thus a type B2-like texture without a melilite mantle would be produced. But this line of reasoning only provided an upper bound on the hydrogen pressure required to produce the type B2 texture. Recall that our original model was that, because a type B2 melt did not form a melilite mantle, it must have maintained contact with the external gas. The expectation was that isotopic fractionation should increase with progressive crystallization, leading to a correlation between isotopic fractionation and our index of crystallization: åkermanite content of the melilite. This is not observed. Therefore, the question becomes: are there conditions such that melt is still exposed at the surface while melilite is crystallizing (i.e., no melilite mantle) and yet do *not* lead to increased isotopic fractionation during the solidification of the interior of a type B2 melt droplet? The seeming negative results of our current study vis-à-vis our expectations actually can be used as a constraint on the evaporation rate and the surrounding hydrogen pressure during melilite crystallization in type B2 melts.

Both the diffusion and the evaporation rate of silicon and magnesium are functions of temperature. As noted above, the evaporation rate also depends on the surrounding hydrogen pressure, increasing as $P_{H_2}^{1/2}$ (Richter et al. 2002). We can use the parameterization of the evaporation kinetics of magnesium given by Richter et al. (2002), and the kinetic fractionation factor for magnesium evaporation given by Richter et al. (2007b) to address the question of the evaporation conditions required in order that little or no evaporation (and associated isotopic fractionation) would take place from a molten type B2 CAI. Temperature is constrained by the fact that melilite crystallizes from a typical type B CAI composition between 1400 and 1250 °C (Stolper 1982). We will use a radius of 0.5 cm in our calculations based on the size of *All TS33* (see Fig. 2). Stolper and Paque (1986) used crystallization experiments to show that at high cooling rates or melting temperatures above the liquidus

temperature of melilite, the melilite will crystallize as dendritic crystals. Therefore (as noted above), the cooling rate is constrained to be no faster than 50 °C h^{-1} to produce the nondendritic melilite grains observed in *All TS33* and all other type B CAIs. Stolper and Paque (1986) estimated the minimum cooling rate to be 0.5 °C h^{-1}. For present purposes, a simple evaporation model for magnesium will be used to place constraints on the conditions that would result in small or negligible evaporation and isotopic fractionation of a CAI such as *All TS33*. A similar argument could be made in terms of silicon evaporation. The conservation equation we use is:

$$\frac{\partial(V\rho_{Mg})}{\partial t} = A\,J_{Mg} \tag{4}$$

where V is the volume of the CAI, ρ_{Mg} is the molar density of magnesium, A is the surface area, and J_{Mg} is the flux of magnesium per unit surface area per unit time (t). The changes of volume and surface area due to evaporation of a small amount of SiO_2 and MgO are negligible in terms of their effect on the isotopic fractionation as a function of time, thus we can assume that V and A are constants. The conservation equation can then be written as

$$\frac{\partial\,\rho_{Mg}}{\partial t} = (3/r)\,J_{Mg} \tag{5}$$

where we have assumed the CAI is a sphere of radius r. The parameterization of the evaporation flux of magnesium as a function of temperature and hydrogen pressure given by Richter et al. (2002) is

$$J(T, P_{H_2}) = J(T_0, P_{0)})\,e^{E/R\,(1/T_0 - 1/T)}\sqrt{\frac{P_{H_2}}{P_0}} \tag{6}$$

where T_0 and P_0 are the temperature and hydrogen pressure at which the evaporation rate is known, E is an activation energy, and R is the gas constant. The final equation that needs to be specified is the magnesium isotopic fractionation of the residue as a function of the amount of magnesium evaporated. Laboratory evaporation experiments (see Richter et al. 2002, 2007b) have shown that the isotopic fractionation of magnesium from a CAI-like melt follows the Rayleigh law, given earlier as Equation 1:

$$R/R_0 = f^{(\alpha-1)} \tag{7}$$

where R is the isotopic ratio in the residue (i.e., $^{25}Mg/^{24}Mg$), R_0 is the isotopic ratio before evaporation,

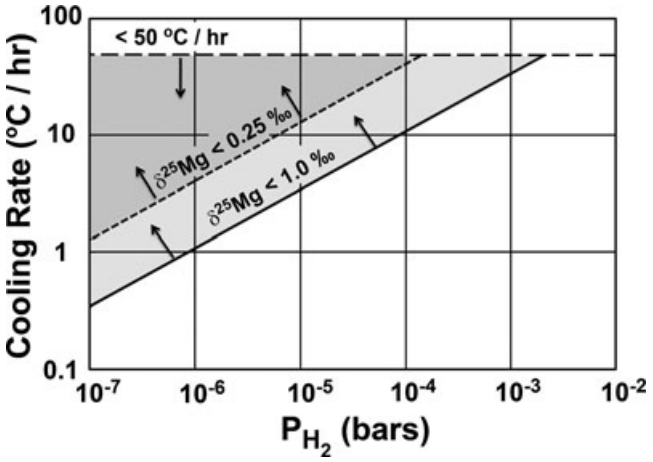

Fig. 9. This figure shows the region in cooling rate—hydrogen pressure space that would allow for the crystallization of euhedral melilite (dT/dt < 50 °C h^{-1} from Stolper and Paque 1986) and magnesium isotopic fractionation of $^{25}Mg/^{24}Mg$ by less than 1‰ (light gray region above the solid line) or less than 0.25‰ (the darker gray region above the dashed line). The shaded regions thus show the conditions in which a type B2 CAI such as *All TS33* could have crystallized euhedral melilite grains with relatively uniform magnesium isotopic composition. The details of the calculation used to construct this figure are given in the text.

f is the fraction of Mg remaining in the residue, and α is the kinetic isotope fractionation factor corresponding the ratio of the isotopic composition of the evaporation flux to that of the evaporating material. The isotopic fractionation in per mil is then

$$\delta^{25}Mg(‰) = 1000\times(R/R_0 - 1) \tag{8}$$

The specific issue we address using Equations (5–7) is the cooling rate as a function of hydrogen pressure such that the calculated magnesium isotopic fractionation of the residue is small (i.e., less than 1‰ or 0.25‰ in $\delta^{25}Mg$). That is, what combination of cooling rate versus hydrogen pressure will result in no significant isotopic fractionation occurring during solidification of the interior of a type B2 CAI. To calculate the cooling rate, we specify ρ_{Mg} = 0.0075 moles Mg cm^{-3} (approximately 10% MgO), r = 0.5 cm, $J(T_0,P_0)$ = 3.0 × 10^{-8} moles Mg cm^{-2} s for T_0 = 1773K, P_0 = 2 × 10^{-4} bars H_2, E = 300 kJ $mole^{-1}$, and α = 0.992. The molar density and size are taken to represent *All TS33*, the values for $J(T_0,P_0)$ and E are taken from Richter et al. (2002), and the value for α is taken from Richter et al. (2007b) for temperatures in the range 1673–1523 K where melilite crystallizes from a type B CAI-like melt (see Richter et al. 2007b for a discussion of how α varies with temperature). Figure 9 shows lines in cooling rate $-P_{H_2}$ space that would result in $\delta^{25}Mg$ = 1‰ (continuous line) and 0.25‰ (dashed line with short

dashes). The horizontal line at a cooling rate of 50 °C h^{-1} (long dashes) is the upper limit of the cooling rate determined by Stolper and Paque (1986). The light gray shaded triangle in the figure is the region in cooling rate—P_{H_2} space that would allow for nondendritic melilite grains fractionated by less than 1‰ in δ^{25}Mg. The smaller darker triangle uses 0.25‰ as the upper bound on δ^{25}Mg. This figure shows that there is a finite region in cooling rate—P_{H_2} space in which a type B2 melt will not incur either significant surface volatilization ($P_{H_2} < 10^{-4}$ bars) or the formation of an internal isotopic gradient, yet satisfy the requirement that the crystallizing melilite be nondendritic in form (cooling rate <50 °C h^{-1}). Under such conditions, a type B1 melilite mantle would not form. Although a type B1 CAI can form at similar cooling rates to those that would produce a type B2 CAI, a higher evaporation rate—and thus a higher hydrogen pressure—would be required to deplete the outer parts of the molten inclusion in silicon and magnesium and thus crystallize melilite at the surface first to produce the diagnostic melilite mantle of the type B1 CAI. In terms of this interpretation, the two variants of type B CAIs mainly reflect differences in the hydrogen pressure (in effect the fO_2) of the surrounding gas during crystallization.

Comments on the Origin of the Outermost Mantle Zones

The outermost 0.5–1 mm of each of these CAIs exhibit steep isotopic gradients independent of whether the CAIs are B1 or B2, and independent also of size of the CAI (e.g., *All TS33* is nearly twice the diameter of *Vig F1*). Our observations differ from those of Shahar and Young (2007) because most of the gradients we observe in our CAIs, especially for magnesium, tend toward being isotopically lighter on the outer margin of the CAI. Thus, this observation would appear to pose a problem for any model that involves surface evaporation during melting of the CAIs, whether that of Richter et al. (2006) or that of Shahar and Young (2007). In the present context, the observation is especially problematic for the model of Richter et al. (2006) that requires evaporation of magnesium and silicon to make B1 mantles. Although in places (but not everywhere) δ^{30}Si is isotopically heavy (relative to the interiors) in this region of three of the CAIs we studied, it is actually lighter in some places at the margin of *AL-4884*; magnesium at the margins is lighter in all four of the CAIs. Yet, there are two independent reasons for thinking that the outer zones of all of our CAIs experienced some kind of surface volatilization. One is the high level of enrichment in δ^{30}Si in their outer margins of three of the CAIs relative to the interiors. The second is that in all four CAIs, the melilite located within 50–100 μm of the very edge of the CAIs is somewhat more aluminous ($Åk_{0–10}$) than expected for the first-crystallized melilite from melts of typical type B compositions (approximately $Åk_{10–20}$; e.g., Stolper 1982; Richter et al. 2006). The latter is suggestive that the anomalously gehlenitic melilites crystallized from a local melt with higher Al/Mg than the bulk CAI composition, due most likely to surface volatilization depleting silicon and magnesium relative to the much more refractory aluminum. This is supported by experiments of Mendybaev et al. (2006) in which mantle melilite of synthetic B1s produced by evaporation of type B CAI melt in hydrogen are more gehlenitic than melilite from the interior. We can think of no process to locally enrich the silicon isotopes in the outer CAI regions other than evaporation; for example, exchange with an external reservoir would require that reservoir to have isotopically heavier silicon than normal solar or the CAI itself. We can only speculate that very localized melt evaporation did in fact occur, but later isotopic exchange of magnesium (and in one case silicon) with an external isotopically normal reservoir affected some of the inclusions in such a way as to reverse what must originally have been heavy isotope enrichment near the CAI margins. In the case of *AL-4884*, this occurred with silicon as well. We recognize that this is an *ad hoc* and, in many ways, unsatisfying model. It is interesting to note that if Shahar and Young (2007) had studied any one of the CAIs we analyzed, they might not have proposed their relatively simple melt evaporation model. By chance, they happened to study one CAI that showed heavy isotopic enrichment of both silicon and magnesium near the margin of their CAI. Why their CAI showed a pattern so different from many of ours is a puzzle that can only be explained by further studies of additional CAIs and more detailed characterization of the outermost layers of isotopically fractionated CAIs.

SUMMARY

Our study of two type B1 and two type B2 CAIs showed that in bulk they are significantly fractionated (heavy) in both magnesium and silicon isotopes, indicating that a significant fraction of their original magnesium (approximately 40–60% depending on the CAI) and silicon (approximately 10–30%) was removed by evaporation. Furthermore, with the exception of the outer ≤1000 μm of each CAI (depending on the element and the CAI), the isotopic compositions of both magnesium and silicon in melilite were found to be effectively uniform as a function of both distance from the surface and the åkermanite content of the melilite. The uniform isotopic composition of the melilite

requires that the loss of magnesium and silicon must have occurred during one or more melting events and prior to crystallization of the now present melilite. This idea is consistent with previous work suggesting multiple melting events in type B CAIs, based on evidence for the existence of sodium in the melt prior to the most recent solidification (MacPherson and Davis 1993; Beckett and Stolper 2000; Simon and Grossman 2006).

The finding that, both in B1 and B2 inclusions, the interior isotopic fractionation patterns are flat as a function of radial distance from the CAI margins is inconsistent with the prediction of Richter et al. (2006) that B2s should show increasing isotopic fractionation with progressive igneous crystallization as tracked by melilite åkermanite content. Our modeling shows that solidification of a type B2 melt can occur without producing an isotopic gradient in the CAI interior provided surface evaporation is sufficiently slow that diffusion maintains a homogeneous melt and that evaporation is also slow compared with the rate of melilite crystallization. This requires a combination of cooling rate versus hydrogen pressure conditions that differ from those under which type B1 CAI solidified: the latter require $P_{H_2} > 10^{-4}$ bars and cooling rates of 10–50 °C h^{-1}, whereas type B2 CAIs require $P_{H_2} < 10^{-4}$ bars at a wider potential range of cooling rates down to values as low as approximately 0.5 °C h^{-1} depending on the hydrogen pressure. If type B2 CAIs can be shown to have cooled significantly slower than approximately 10 °C h^{-1}, the required hydrogen pressures (essentially equal to total nebular pressure) are substantially lower than those commonly assumed for equilibrium condensation calculations (e.g., Grossman 1972; Yoneda and Grossman 1995). This means that the cooling rates of type B2 CAIs represent a potential cosmobarometer, and further constraining those cooling rates is an important avenue for future investigation.

Acknowledgments—The manuscript was greatly improved by careful and thoughtful reviews by Drs. Christine Floss (Assoc. Ed.), Yunbin Guan, Julie Paque, and Steve Simon. This work was supported by NASA grants NNX09AG39G (A. M. D., PI), NNX09AB88G (N. K., PI), NNX11AD43G (G. J. M., PI), and NNX09AG38G (F. R., PI). WiscSIMS is partly supported by NSF (EAR03-19230, EAR07-44079).

Editorial Handling—Dr. Christine Floss

REFERENCES

Beckett J. R. 1986. The origin of calcium-aluminum-rich inclusions from carbonaceous chondrites: An experimental study. Ph.D. Thesis. University of Chicago, Chicago, Illinois. 373 p.

Beckett J. R. and Stolper E. 2000. The partitioning of Na between melilite and liquid: Part I. The role of crystal chemistry and liquid composition. *Geochimica et Cosmochimica Acta* 64:2509–2517.

Bullock E. S., MacPherson G. J., Nagashima K., Krot A. N., Petaev M. I., Jacobsen S. B., and Ulyanov A. A. 2012. Forsterite-bearing type B refractory inclusions from CV3 chondrites: From aggregates to volatilized melt droplets. *Meteoritics & Planetary Science* 47:2128–2147, doi:10.1111/j.1945-5100.2012.01396.x.

Clayton R. N., Mayeda T. K., and Molini-Velsko C. 1985. Isotopic variations in solar system material: Evaporation and condensation of silicates. In *Protostars and planets II*, edited by Black D. C. and Shapley Mathews M. Tucson, Arizona: University of Arizona Press. pp. 755–771.

Clayton R. N., Hinton R. W., and Davis A. M. 1988. Isotopic variations in the rock-forming elements in meteorites. *Philosophical Transactions of the Royal Society of London* 325:483–501.

Davis A. M., Hashimoto A., Clayton R. N., and Mayeda T. K. 1990. Isotope mass fractionation during evaporation of Mg_2SiO_4. *Nature* 347:655–658.

Grossman L. 1972. Condensation in the primitive solar nebula. *Geochimica et Cosmochimica Acta* 36:597–619.

Grossman L., Ebel D. S., Simon S. B., Davis A. M., Richter F. M., and Parsad N. M. 2000. Major element chemical and isotopic compositions of refractory inclusions in C3 chondrites: The separate roles of condensation and evaporation. *Geochimica et Cosmochimica Acta* 64:2879–2894.

Grossman L., Simon S. B., Rai V. K., Thiemens M. H., Hutcheon I. D., Williams R. W., Galy A., Ding T., Fedkin A. V., Clayton R. N., and Mayeda T. K. 2008. Primordial compositions of refractory inclusions. *Geochimica et Cosmochimica Acta* 72:3001–3021.

Heck P. R., Huberty J. M., Kita N. T., Ushikubo T., Kozdon R., and Valley J. W. 2011. SIMS analyses of silicon and oxygen isotope ratios for quartz from Archean and Paleoproterozoic banded iron formations. *Geochimica et Cosmochimica Acta* 75:5879–5891.

Kita N. T., Ushikubo T., Knight K. B., Mendybaev R. A., Davis A. M., Richter F. M., and Fournelle J. H. 2012. Internal ^{26}Al-^{26}Mg isotope systematics of a type B CAI: Remelting of refractory precursor solids. *Geochimica et Cosmochimica Acta* 86:37–51.

Knight K. B., Kita N. T., Mendybaev R. A., Richter F. M., Davis A. M., and Valley J. W. 2009a. Silicon isotopic fractionation of CAI-like vacuum evaporation residues. *Geochimica et Cosmochimica Acta* 73:6390–6401.

Knight K. B., Kita N. T., Richter F. M., Davis A. M., and Mendybaev R. A. 2009b. Mg and Si isotope fractionation within three type B Ca-Al-rich inclusions (abstract #2360). 40th Lunar and Planetary Science Conference. CD-ROM.

MacPherson G. J. 2007. Calcium-aluminum-rich inclusions in chondritic meteorites. In *Meteorites, comets, and planets*, edited by Holland H. D. and Turekian K. K. Treatise on Geochemistry, vol. 1. Oxford: Elsevier.

MacPherson G. J. and Davis A. M. 1993. A petrologic and ion microprobe study of a Vigarano type B2 refractory inclusion: Evolution by multiple stages of melting and alteration. *Geochimica et Cosmochimica Acta* 57:231–243.

MacPherson G. J. and Grossman L. 1981. A once-molten, coarse-grained, Ca-rich inclusion in Allende. *Earth and Planetary Science Letters* 52:16–24.

MacPherson G. J., Paque J. M., Stolper E., and Grossman L. 1984. The origin and significance of reverse zoning in melilite from Allende type B inclusions. *Journal of Geology* 92:289–305.

MacPherson G. J., Kita N. T., Ushikubo T., Bullock E. S., and Davis A. M. 2012. Well-resolved variations in the formation ages for Ca-Al-rich inclusions in the early solar system. *Earth and Planetary Science Letters* 331:43–54.

Mendybaev R. A., Richter F. M., and Davis A. M. 2006. Crystallization of melilite from CMAS-liquids and the formation of the melilite mantle of type B1 CAIs: Experimental simulations. *Geochimica et Cosmochimica Acta* 70:2622–2642.

Mendybaev R. A., Davis A. M., Richter F. M., and Ebel D. S. 2007. Melilite from synthetic and natural type B CAIs: Similarities and differences (abstract #2329). 38th Lunar and Planetary Science Conference. CD-ROM.

Richter F. M., Davis A. M., Ebel D. S., and Hashimoto A. 2002. Elemental and isotopic fractionation of type B calcium-, aluminum-rich inclusions: Experiments, theoretical considerations, and constraints on their thermal evolution. *Geochimica et Cosmochimica Acta* 66:521–540.

Richter F. M., Mendybaev R. A., and Davis A. M. 2006. Conditions in the protoplanetary disk as seen by the type B CAIs. *Meteoritics* 41:83–93.

Richter F. M., Kita N. T., Mendybaev R. A., Davis A. M., and Valley J. W. 2007a. High-precision Mg isotopic composition of type B1 and B2 CAI melilite (abstract #2303). 38th Lunar and Planetary Science Conference. CD-ROM.

Richter F. M., Janney P. E., Mendybaev R. A., Davis A. M., and Wadhwa M. 2007b. Elemental and isotopic fractionation of type B CAI-like liquids by evaporation. *Geochimica et Cosmochimica Acta* 71:5544–5564.

Shahar A. and Young E. D. 2007. Astrophysics of CAI formation as revealed by silicon isotope LA-MC-ICPMS of an igneous CAI. *Earth and Planetary Science Letters* 257:497–510.

Simon S. B. and Grossman L. 2006. A comparative study of melilite and fassaite in types B1 and B2 refractory inclusions. *Geochimica et Cosmochimica Acta* 70:780–798.

Simon S. B., Grossman L., and Davis A. M. 1991. Fassaite composition trends during crystallization of Allende type B refractory inclusions. *Geochimica et Cosmochimica Acta* 55:2635–2655.

Stolper E. 1982. Crystallization sequences of Ca-Al-rich inclusions from Allende—An experimental study. *Geochimica et Cosmochimica Acta* 46:2159–2180.

Stolper E. and Paque J. M. 1986. Crystallization sequences of Ca-Al-rich inclusions from Allende: The effects of cooling rate and maximum temperature. *Geochimica et Cosmochimica Acta* 50:1785–1806.

Sugiura N., Mizuno T., Ushikubo T., and Hiyagon H. 2004. Si and Mg isotope fractionations in melilite in coarse-grained CAIs measured by SIMS. *Geochemical Journal* 38:405–415.

Wark D. A., and Lovering J. F. 1977. Marker events in the early evolution of the solar system—Evidence from rims on Ca-Al-rich inclusions in carbonaceous chondrites. Proceedings, 1st Lunar Science Conference. pp. 95–112.

Wark D. A. and Lovering J. F. 1982. The nature and origin of type B1 and B2 inclusions in the Allende meteorite. *Geochimica et Cosmochimica Acta* 46:2581–2594.

Wark D. A., Boynton W. V., Keays R. R., and Palme H. 1987. Trace element and petrologic clues to the formation of forsterite-bearing Ca-Al-rich inclusions in the Allende meteorite. *Geochimica et Cosmochimica Acta* 51:607–622.

Yoneda S. and Grossman L. 1995. Condensation of CaO-MgO-Al_2O_3-SiO_2 liquids from cosmic gases. *Geochimica et Cosmochimica Acta* 59:3413–3444.

SUPPORTING INFORMATION

Additional supporting information may be found in the online version of this article:

Table S1: Magnesium isotopic composition, mol% Åk, and distance from rim of each analytical spot from rim in *Leo 3535-1, AL-4884, All TS33*, and *Vig F1*.

Table S2: Silicon isotopic composition, mol% Åk, and distance from rim of each analytical spot from rim in *Leo 3535-1, AL-4884, All TS33*, and *Vig F1*.

Fig S1: Back-scattered electron (BSE) image of *Leo 3535-1*, with colored quantitative maps of melilite åkermanite content (mole%). The locations of silicon isotopic analyses are indicated by white squares.

Fig S2: Back-scattered electron (BSE) image of *Leo 3535-1*. The locations of magnesium isotopic analyses are indicated by red circles.

Fig S3: Back-scattered electron (BSE) image of *AL-4884*, with colored quantitative maps of melilite åkermanite content (mole%). The locations of silicon and magnesium isotopic analyses are indicated by white squares and red circles, respectively.

Fig S4: Back-scattered electron (BSE) image of *All TS33*, with colored quantitative maps of melilite åkermanite content (mole%). The locations of silicon and magnesium isotopic analyses are indicated by white squares and red circles, respectively.

Fig S5: Back-scattered electron (BSE) image of *Vig F1a*, with colored quantitative maps of melilite åkermanite content (mole%). The locations of silicon and magnesium isotopic analyses are indicated by white squares and red circles, respectively.

Fig S6: Back-scattered electron (BSE) image of *Vig F1b*, with colored quantitative maps of melilite åkermanite content (mole%). The locations of silicon and magnesium isotopic analyses are indicated by white squares and red circles, respectively.